ADVANCED MATERIALS TECHNOLOGIES
www.advmattechnol.de

High-Conductivity Crack-Free 3D Electrical Interconnects Directly Printed on Soft PDMS Substrates

Jacob Brenneman, Derya Z. Tansel, Gary K. Fedder, and Rahul Panat**

Nanoparticle 3D printing and sintering is a promising method to achieve freeform interconnects on compliant substrates for applications such as soft robotics and wearable healthcare devices. However, previous strategies to sinter metallic nanoparticles while preserving the soft polymer substrate are rife with problems such as cracking and low conductivity of the metallic features. In this paper, the mechanisms of cracking in nanoparticle-based 3D printed and sintered stretchable interconnects are identified and architecture and processing strategies are demonstrated to achieve crack-free interconnects fully embedded in thin (<100 µm in thickness) stretchable polydimethylsiloxane (PDMS) with external connectivity. Capillary forces between nanoparticles developed through rapid solvent evaporation in the colloidal ink is hypothesized to initiate cracking during drying. Additionally, the presence of oxygen promotes the removal of organic surfactants and binders in the nanoparticle ink which increases nanoparticle agglomeration, grain growth, and subsequently conductivity. An experimental step-wise variation of the thermal/atmospheric process conditions supports this hypothesis and shows that the presence of air during a low temperature drying step reduces the capillary stress to produce crack-free interconnects with high conductivities (up to 56% of bulk metal) while having an excellent compatibility with the underlying polymer materials. Finally, stretchable interconnects fully-encapsulated in PDMS polymer, with 3D pillar architectures for external connectivity are demonstrated, thus also solving an important "last-mile" problem in the packaging of stretchable electronics.

J. Brenneman, R. Panat
Department of Mechanical Engineering
Carnegie Mellon University
Pittsburgh, PA 15213, USA
E-mail: rpanat@andrew.cmu.edu

D. Z. Tansel, G. K. Fedder
Department of Electrical and Computer Engineering
Carnegie Mellon University
Pittsburgh, PA 15213, USA
E-mail: fedder@cmu.edu

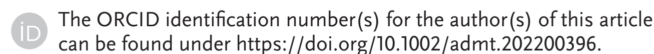
The ORCID identification number(s) for the author(s) of this article can be found under https://doi.org/10.1002/admt.202200396.

© 2022 The Authors. Advanced Materials Technologies published by Wiley-VCH GmbH. This is an open access article under the terms of the Creative Commons Attribution-NonCommercial License, which permits use, distribution and reproduction in any medium, provided the original work is properly cited and is not used for commercial purposes.

DOI: 10.1002/admt.202200396

1. Introduction

Stretchable electronics are increasingly necessary for use in fields such as health monitoring devices,[1] soft robotics,[2] and human machine interfaces[3] due to their elastic modulus match with biological tissue. Epidermal electronic devices have been investigated widely, with recent advancements including a variety of sensors capable of wireless data and power transfer while conforming and stretching with sensitive skin.[4] In addition to epidermal devices, prototype stretchable electronics have been developed to wirelessly monitor aneurysms in arteries.[5] Printing methods offer an attractive alternative to expensive lithographic techniques typically used for the fabrication of stretchable devices due to the low cost of operation, rapid prototyping, and an ability to scale fabrication to a roll-to-roll process.[6–7]

Printing methods such as aerosol jet, inkjet, screen printing, and extrusion printing typically use metallic inks composed of colloidal nanoparticles to create functional devices. Additional ink formulations include dispersed metallic nanowires,[8] carbon nanotubes,[9] or particle free metal–organic decomposition (MOD) inks.[10] Printed colloidal inks must be sintered to achieve conductivity. Thermal sintering is the most common method to achieve conductivity, with higher temperatures and longer exposure times generally yielding films with higher conductivity.[11] However, directly printed conductors on flexible and stretchable substrates are usually sintered at lower temperatures to preserve the stretchable (polymer) substrate, resulting in lower conductivities and stiffer material properties.[12–13] Several methods have been investigated to sinter metallic nanoparticles without damaging the substrate materials including pulsed laser,[14–15] microwave,[16] chemical,[17] flash sintering,[18–19] or plasma sintering.[20] Additionally, the ink composition can be tuned to reduce the sintering temperature to achieve high conductivity by changing the nanoparticle size and nanoparticle capping materials to promote sintering at lower temperatures.[21–22] Regardless of the type of sintering method used, flexible interconnect systems are accompanied with engineering strategies such as discontinuous interlayers[23–24] or serpentine or self-similar geometries[25] to prevent cracking in the conductive layer due to its elastic modulus

mismatch with the soft substrate. Additionally, intermediate layers (with intermediate elastic moduli) have been utilized to reduce stiffness gradients and prevent cracking.[26–27]

Previous work has shown that utilizing inert or vacuum environments can preserve a commonly used elastomer substrate, polydimethylsiloxane (PDMS), up to temperatures as high as 300 °C, while maintaining its stretchability.[28] This would allow for thermal sintering of the metallic conductor consistent with the process temperatures capable of fabricating complex 3D structures including lattices, wavy plates, and pillar structures directly on the stretchable substrate.[29–30] This capability can open a wide design space for stretchable electronics that will pave the way for multilayered stretchable circuits, targeted epidermal contact, wireless data and power transfer, and external wired connections. However, inert ambient environments have been shown to decrease the removal of the organic capping ligands and binders, which is required before sintering can occur in metallic nanoparticle inks.[17,31–33] Cracking in colloidal inks is also a common occurrence,[34–37] and several models have linked an increase in the solvent evaporation rate to an increase in cracking due to the capillary pressure, which leads to increased tensile stress in the drying film.[38–40]

This research is undertaken to demonstrate a fabrication method to create directly printed crack-free interconnects with 3D features for external connectivity. The focus was on understanding the mechanisms of interconnect cracking that would guide mitigation strategies and understanding microstructure development during sintering of colloidal nanoparticle inks to increase electrical conductivity, while also maintaining process conditions that are compatible with PDMS, a common stretchable electronics substrate. We hypothesized that cracking occurs due to capillary pressure during drying and sintering steps and that organics in the nanoparticle ink need to be effectively removed to promote sintering. A hybrid process starting with a drying step under air followed by a high temperature vacuum sintering process is shown to eliminate cracking and increase the electrical conductivity. Shear tests are carried out to demonstrate the robustness of printed pillars that act as conductive connections to the external environment, while an adhesion test is used to establish adequate bonding between the top and the bottom PDMS layers encapsulating the interconnects. Utilizing these learnings, an embedded 3D stretchable interconnect directly printed on PDMS with high conductivity and no cracks is demonstrated. As a verification of function, system stretchability up to 30% strain for a resistance change within 2% of the baseline is shown.

2. Results and Discussion

The 3D stretchable electronic interconnect consisted of aerosol jet printed (AJP) silver interconnects encapsulated by top and bottom (PI) layers and fully embedded within PDMS except for the exposed tips of the pillars, which enable external connection. The schematics of the sample construction and the fabrication process steps are given in **Figure 1**A,B, respectively. The presence of PI between silver and PDMS creates a stiffness gradient due to its intermediate modulus value. Incorporating such a stiffness gradient is known to lower the strain gradient during processing and operation, reducing cracking.[26–27] In fact, we originally printed Ag directly on a PDMS substrate, which resulted in cracks in the Ag interconnects after sintering. A typical result is included in Figure S1 of the Supporting Information. The interconnects and the pillars used for external connection are fabricated by a layer-by-layer AJP process. The layout of the printed samples is given in Figure 1C. Different pillar designs for external connection are shown in Figure 1D–G. These pillars can be printed with heights ranging from tens of micrometers to more than a millimeter using a droplet-based point-wise printing method previously developed by the authors.[12,29] Two different pillar designs were selected to focus on this work and include the circular hollow pillar (Figure 1D), and the tapered full pillar (Figure 1E).

Pretreatment of the PDMS, curing of the PI layers, and sintering of the Ag layer was conducted inside of a vacuum chamber with programmable temperature ramp rates and holding steps capable of reaching 300 °C and 0.13 Pa vacuum with either air or N_2 as the filler gas. The curing and sintering process conditions for PI and Ag, respectively, were kept the same to minimize underlying material changes during subsequent curing and sintering steps but were varied between samples to investigate the effect of process changes on the cracking and conductivity of the silver layer. The initial thermal treatment carried out under vacuum conditions is shown in **Figure 2**A, including a drying step that was incorporated to prevent delamination between the PI layers (an outcome of our previous work[41]). The hybrid process starting with drying under air followed by sintering under vacuum conditions is shown in Figure 2B. The process conditions are summarized in **Table 1**, where experiment #2 and #17 correlate with the processes shown in Figure 2A and 2B, respectively.

Table 1 shows the printed and sintered silver interconnect lines fabricated using 18 different process conditions evaluated in this work. For each process condition, the conductivity is reported as the average of measurements from four interconnects shown in Figure 1C, along with crack observations and compatibility with PDMS. Many of the test samples did not have the PDMS or (poly(acrylic acid) (PAA) release layer present as they were only used for process development. For process conditions 1–5 in Table 1, the printed samples underwent vacuum sintering during the drying step at the beginning of the thermal treatment and all displayed cracking as shown in **Figure 3**; and Figure S2 (Supporting Information). The cracking primarily occurred at the base of the pillars in both the example pillar shapes printed as shown in Figure 3A–D for the tapered pillar, and Figure S2A–D (Supporting Information) for the hollow straight pillar. These cracking images show that the crack extends fully through the layer of silver and develops a significant separation distance from the originally connected surfaces as shown in Figure 3C; and Figure S2C (Supporting Information). In some severe cracking cases, such as conditions 1 and 3 in Table 1, the cracking occurred at the transition from the pillar pad to the interconnect traces as shown in **Figure 4**. Additionally, samples that were under vacuum or inert environment for the entirety of the thermal treatment resulted in low conductivity for process conditions 1–9 in Table 1. This low conductivity is not caused by the cracks shown in Figure 3; and Figure S2 (Supporting Information),

© 2022 The Authors. Advanced Materials Technologies published by Wiley-VCH GmbH

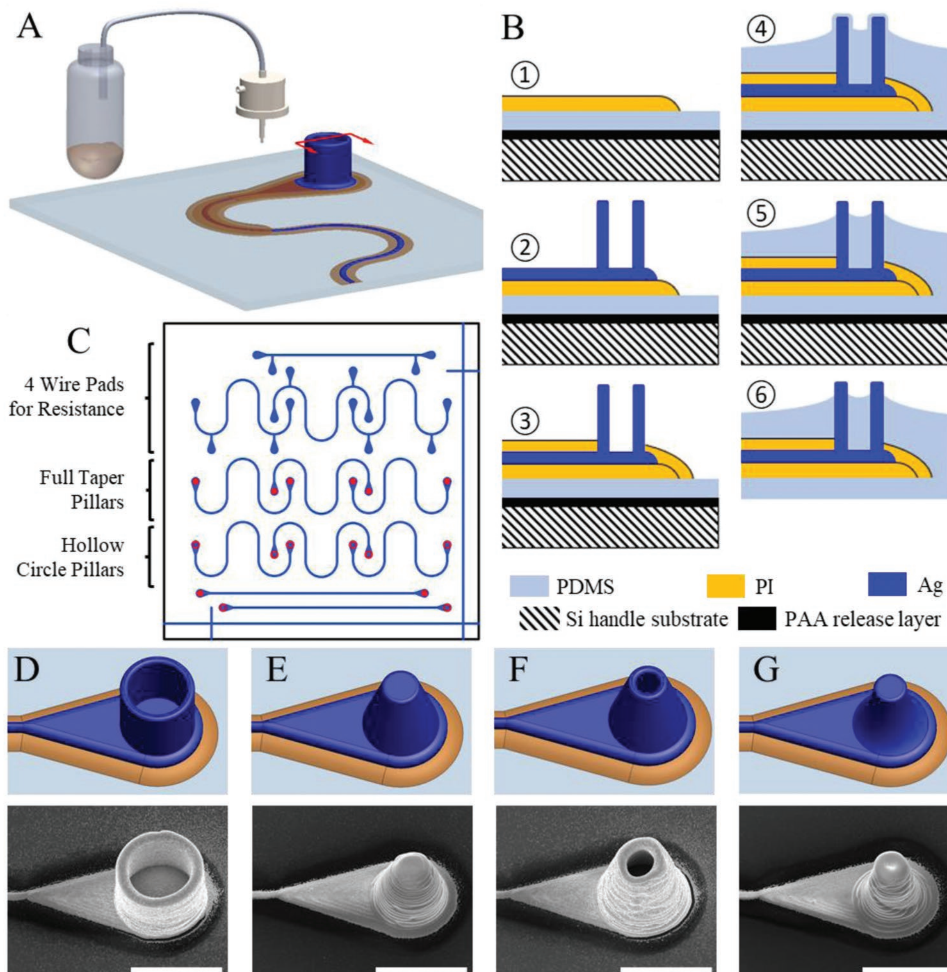

Figure 1. Aerosol jet printing process schematic, fabrication steps, sample layout, and pillar geometries. A) Schematic of AJP where the second layer of PI is being deposited. The cutout view for the fabrication steps is shown by the arrows. The fabrication printing process B) starts with (1) printing the first layer of PI directly onto PDMS substrate which has been spun coated on top of a Si handle substrate with a polyacrylic acid (PAA) release layer. The PI is cured and then (2) Ag interconnects and pillars are printed in a layer-by-layer process on top of first PI layer. Ag is sintered and (3) the second PI layer is printed and cured. (4) PDMS is spun coated to encapsulate everything. (5) Timed wet etch of PDMS to expose the pillar tips. (6) Release sample with saline soak. C) The sample layout where the four repeated samples are shown for the hollow circle pillars, full taper pillars, and the four-wire resistance samples for precise conductivity measurements. Each sample set is printed on a $\times$ 1 cm^2 wafer and has three meander interconnects and one straight interconnect. Renderings and SEM images of fabricated geometries are shown in D–G) where the D) hollow circular pillar and E) taper pillar were included in the sample set for this study and the F) hollow taper pillar and G) curved taper pillar are shown as further possibilities. Scale bars in D–G) are 200 µm.

and 4 as the four-wire resistance test features used to determine the conductivity did not display cracks at the pad to trace transition or along the trace section measured by the multimeter and shown in Figure 1C. The vacuum sintering process initially showed promise as a path to achieve high temperature sintering without damaging the stretchable PDMS substrate but displayed unacceptable drawbacks in causing both cracking and low conductivity in the sintered silver interconnect traces. A hybrid process was developed where the drying step was performed under air at atmospheric pressure followed by a high temperature treatment under vacuum to produce conductivities as high as 56% of bulk silver (process condition 14 in Table 1) while retaining the stretchability of the PDMS substrate. The cause of both the cracking behavior and low conductivity is discussed in the following sections along with the proposed process solution to achieve high conductive and crack free 3D printed features directly printed on a PDMS substrate.

2.1. Cracks

Figure 3; and Figure S2 (Supporting Information) shows cracking at the transition of the pillar and pad region in both the tapered and hollow circular pillars when the samples were dried under vacuum. Focused Ion Beam (FIB) cuts were made to image the cross section of the crack to investigate the crack morphology. Close-up images of the crack (Figure 3C; and Figure S2C, Supporting Information) show that the crack extends through the entire layer of the silver with a separation of 3.2 µm for the taper pillar and 4.0 µm for the circular pillar, indicating mode-I fracture. Additionally, the silver layer

© 2022 The Authors. Advanced Materials Technologies published by Wiley-VCH GmbH

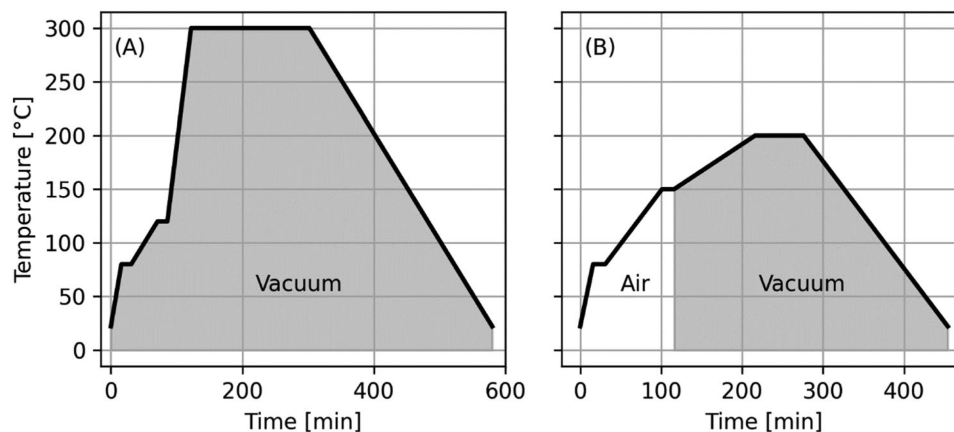

Figure 2. Process engineering to achieve crack-free and high-conductivity interconnects direct printed on PDMS. A) First prototype sintering thermal profile that caused low conductivity and cracking. B) The proposed profile to achieve simultaneous elastic PDMS and high conductivity and crack free interconnects and pillars. The process conditions in (A) and (B) correspond to those for experiment #2 and #17 in Table 1, respectively.

delaminates from the substrate in both the taper pillar and circular pillar geometry as the crack extends underneath the pillar displaying shear or mode-II fracture as shown in Figure 3D; and Figure S2D (Supporting Information). The delamination distance under the tapered pillar is over 18 µm and continues out of the field of view of the image. Under the hollow circular pillar, the delamination distance was measured to be 28 µm, which extends approximately halfway under the thickness of the pillar wall! The delamination also occurred under the meandering interconnect side of the crack as well, but not to the same extent as under the pillar. In addition to cracking at the pillar base, the process condition for experiment #1 and #3

Table 1. Sintering process conditions and the resulting conductivity, cracking description and whether the process is compatible with printing directly onto PDMS substrate.

Experiment	Sample substrate	Drying step			Sintering step				Observations			Problem
		Pressure [kPa]	Gas [–]	Max temp [°C]	Pressure [kPa]	Gas [–]	Max temp [°C]	Ramp rate [°C min^{-1}]	Conductivity [%] of Bulk Ag	Cracks	Compatible with PDMS	
1	Si	–	–	–	0.13	N_2	300	5	0.00 008%	Severe	Yes	Cracking
2	Si	0.13	N_2	120	0.13	N_2	300	5	0.28%	Severe	Yes	Cracking
3	Si	0.13	N_2	150	0.13	N_2	300	5	0.06%	Severe	Yes	Cracking
4	Si	0.13	N_2	120	0.13	N_2	300	0.5	2%	Severe	Yes	Cracking
5	Si	0.13	N_2	120	0.13	N_2	300	0.5	1%	Severe	Yes	Cracking
6	Si	101	N_2	120	101	N_2	300	5	29%	Minor	No	Cracking
7	Si	101[a]	N_2	120	101	N_2	300	5	28%	Moderate	No	Cracking
8	Si	101	N_2	120	101	N_2	300	5	16%	Moderate	No	Cracking
9	Si	101	N_2	120	101	N_2	300	0.5	24%	None	No	Incompatibility with PDMS
10	Si	101	Air	120	101	Air	300	5	62%	None	No	Incompatibility with PDMS
11	Si	101	Air	120	101	Air	300	5	67%	None	No	Incompatibility with PDMS
12	Si	101	Air	150	101	Air	200	5	33.3%[b] 64.3%[c]	None	No	Incompatibility with PDMS
13	Si	101	Air	150	101	Air	200	5	59%	None	No	Incompatibility with PDMS
14	Si	101	Air	150	0.13	N_2	300	5	56%	None	Yes	None
15	Si	101	Air	150	0.13	N_2	200	5	39%	None	Yes	None
16	PDMS+ PAA+Si	101	Air	150	0.13	N_2	200	5	25%	None	Yes	None
17	PDMS+ PAA+Si	101	Air	150	0.13	N_2	200	0.5	37%	None	Yes	None
18	PDMS+ PAA+Si	101	Air	150	0.13	N_2	300	5	43%	None	Yes	None

[a]Included a vacuum purge step; [b]Conductivity after the drying step; [c]Conductivity after the sintering step.

© 2022 The Authors. Advanced Materials Technologies published by Wiley-VCH GmbH

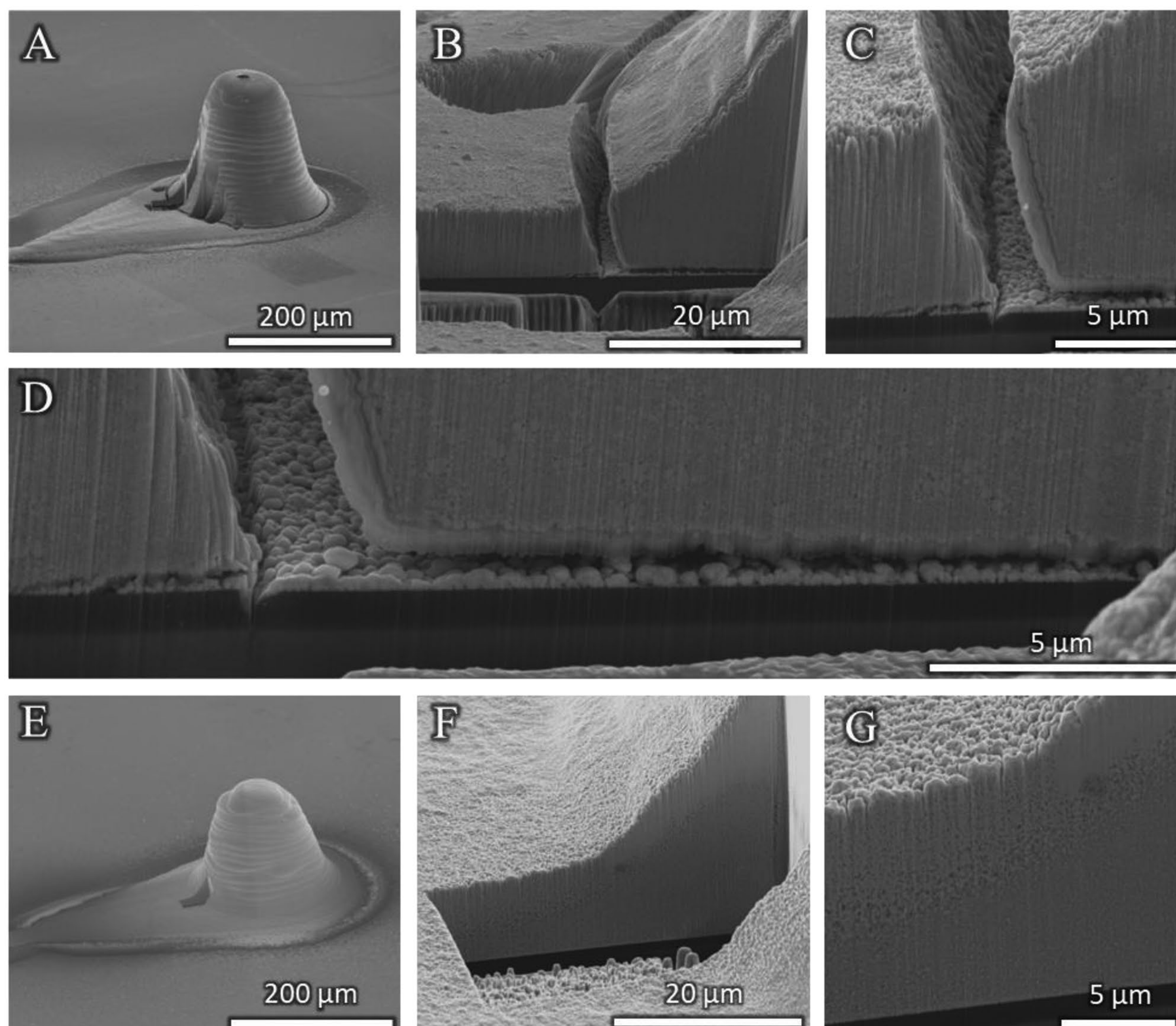

Figure 3. SEM images of uncracked and cracked tapered pillar geometry with FIB cross sections. A–D) A cracked taper pillar with FIB cross section when sintered under process 2. E–G) An uncracked taper pillar with FIB cross section to verify no internal cracking when sintered under process conditions for experiment #13 (Table 1).

(Table 1) produced cracks at the transition from pillar pad to interconnect traces as shown in Figure 4.

The location of the cracks at sharp geometric transitions such as the pillar base (Figure 3; and Figure S2, Supporting Information) and the pad-to-interconnect boundary (Figure 4), but not on the meandering interconnects, indicates that local stress concentration is important for crack initiation. We note that thermal expansion mismatch between the different materials would cause a residual stress during thermal cycling. The thermal expansion mismatch, however, is unlikely to be the driving force for cracking in the current work, as all samples subjected to the same thermal profile should demonstrate similar cracking behavior, which is not observed in the current work (e.g., for samples subjected to similar thermal histories, cracking is observed only in the samples subjected to vacuum and nitrogen environments in the initial drying step). This assessment led to the hypothesis that the increased solvent evaporation rate in vacuum and nitrogen relative to air increased the local stress capable of initiating cracks in the drying of the packed particle bed.

Cracking in printed metallic nanoparticle (NP) inks has been observed across printing techniques including extrusion,[34] inkjet,[36] and aerosol jet printing.[35] We note that cracking during drying of thin films of colloidal dispersions is a well-documented phenomenon and the consensus is that the driving force for cracking is the capillary pressure between particles developed during drying as depicted in **Figure 5**B.[42–43] Several models have been proposed to describe the capillary pressure and resultant film stress and have shown reasonable agreement with experiments with silica colloids.[44] This negative capillary pressure results in a force to pull the nanoparticles together, and when the film is constrained on the substrate, it causes an in-plane tension in the film, which can be relieved by fully drying or cracking (see Figure 5B). The capillary pressure has

 © 2022 The Authors. Advanced Materials Technologies published by Wiley-VCH GmbH

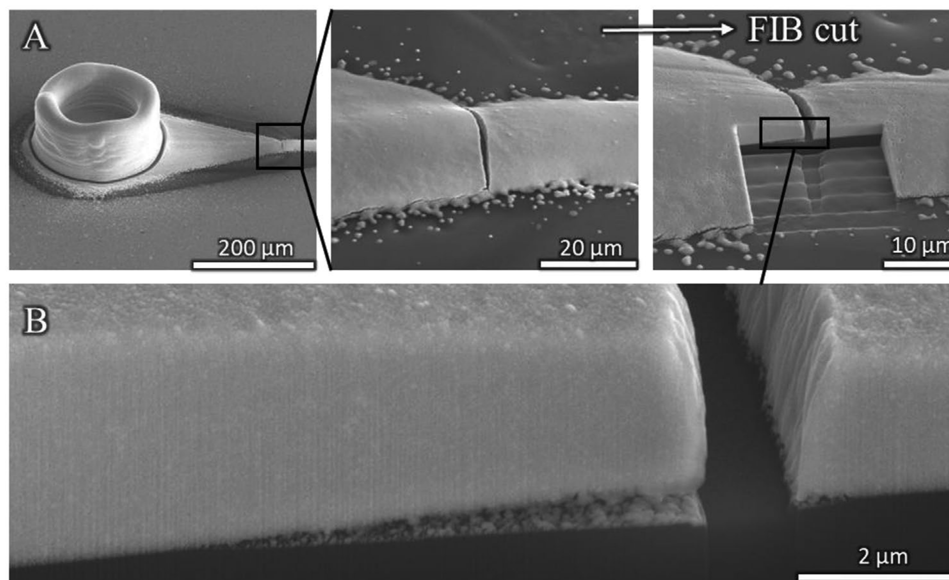

Figure 4. Crack at the pillar pad to interconnect transition. A) SEM image of the pillar, pad, and interconnect resulting from process conditions for experiment #3, where the inset images show close-ups of the interconnect transition, and the FIB cut location. B) SEM image of the FIB cut cross section.

a maximum achievable value $P_{max} = 10\gamma/R$ where γ is the surface tension and R is the particle radius.[42] The actual capillary pressure P developed in the consolidated region is determined by the film thickness, evaporation rate, and the permeability of the film and is limited to magnitudes less than P_{max}. Salamanca et al.[45] describe the dimensionless capillary pressure P_{cap} as the ratio of the maximum capillary pressure to the developed capillary pressure as

$$P_{cap} = \frac{20}{75}\left(\frac{3\gamma\eta_0}{\dot{E}}\right)^{1/2}\frac{R(1-\phi)^2}{\mu\phi^2 H} \tag{1}$$

where η_0 is the dispersion low shear viscosity, $\dot{E}$ is the evaporation rate, ϕ is the volume fraction of particles at close packing, μ is the solvent viscosity, and H is the initial film thickness. Manipulation of Equation (1) returns the capillary pressure developed in the film as

$$P = \frac{75}{2}\left(\frac{\dot{E}\gamma}{3\eta_0}\right)^{1/2}\frac{\mu\phi^2 H}{R^2(1-\phi)^2} \tag{2}$$

The developed in-plane tensile stress, σ, is directly proportional to the capillary pressure, which leads to the ability to compare the film stress for different process conditions. The initial film thickness is the same for all samples and the volume fraction of the particles at consolidation is also assumed to be independent of sintering ambient environment. The low shear viscosity of the dispersion is a function of the volume fraction

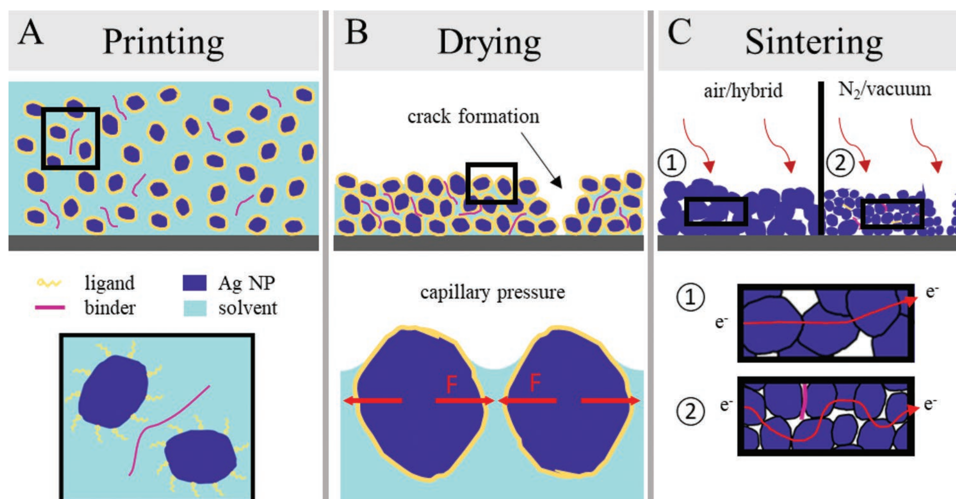

Figure 5. Schematic of process steps for electrical functionalization of colloidal nanoparticle ink. A) The as-printed colloidal ink, where the inset shows the composition of the ink. B) The drying step where the inset image shows the development of capillary pressure. C) The sintering step where the two inset images compare electron pathways between ink sintered in air vs nitrogen and vacuum environments.

© 2022 The Authors. Advanced Materials Technologies published by Wiley-VCH GmbH

directly scaled by the solvent viscosity. Thus, following the assumption that volume fraction at close packing is the same for all samples, a comparison of in-plane tensile stress can be made that includes only the evaporation rate, surface tension, and solvent viscosity, as

$$\frac{\sigma_{\text{vac}}}{\sigma_{\text{air}}} = \left(\frac{\dot{E}_{\text{vac}}\gamma_{\text{vac}}\mu_{\text{vac}}}{\dot{E}_{\text{air}}\gamma_{\text{air}}\mu_{\text{air}}} \right)^{1/2} \tag{3}$$

Equation (3) compares the film stress developed in vacuum with that developed in air; and can also be used to compare the stress between different conditions. The surface tension and the solvent viscosity are temperature dependent, so differences in solvent evaporation rate will determine the temperature at which the film consolidates and develops capillary pressure, which may be different for the different sintering conditions. As temperature increases, both the viscosity and the surface tension decrease, thereby reducing the tensile stress in Equation (3) at the point of consolidation.

From Figures 3 and 4 and Table 1, both the vacuum and N_2 conditions resulted in cracking at the pillar base (with the exception of process condition for experiment #9 in Table 1), while all samples sintered in air were crack-free. Utilizing Equation (3), a comparison of the film stress can be made between the process conditions by estimating the solvent evaporation rate during film consolidation and close packing. The solvent for the ink used in this study comprises water and ethylene glycol, and the significantly lower vapor pressure of ethylene glycol (12 Pa) versus water (3200 Pa) at 25 °C leads to the assumption that at close packing, only ethylene glycol remains as the solvent.[46] Measured evaporation rates for ethylene glycol with process conditions closely matching the ones used in this study are available for vacuum,[47] atmospheric pressure N_2 with gas flow,[48] and atmospheric pressure air.[49] The Hertz–Knudsen equation was used to scale evaporation rates to the same temperature of 25 °C, and are reported to be 52, 1.3, and 0.10 mg min^{-1} cm^{-2} for vacuum, 101 kPa N_2, and air environments, respectively. These evaporation rates are for pure liquid. Although the presence of nanoparticles, ligands, and binders is expected to affect the absolute values of the evaporation rates, their relative rates can still be estimated to compare tensile film stress under different process conditions. Using Equation (3) and the reported evaporation rates, the film stress developed during drying under the N_2 environment is 3.4 times higher than in air, and the film stress developed in vacuum is 23 times higher than that in air. The significantly larger stress developed in vacuum conditions during drying is consistent with the experimental observations and supports the hypothesis that the cracking is caused by capillary stress developed during drying. The increased drying stress in N_2 relative to air is also indicative of drying stress driving the crack for the interconnect. Of the four samples dried under 101 kPa N_2 environment, three displayed complete cracks through the thickness of the silver, while the fourth displayed a minor crack. These observations indicate the stress developed in drying under 101 kPa N_2 environment, local to the pillar base, is close to the critical stress required to initiate crack growth in a packed particle film. When samples underwent the drying step under air followed by vacuum for sintering, such as in experiments #14–18 in Table 1, no cracking was observed, which further indicates that the cracks were initiated in the drying portion of the process.

In addition to the cracks perpendicular to the substrate, we also saw delamination cracks along the interface between the interconnect and the polyimide (Figures 3D and 4B; and Figure S2D, Supporting Information). These are mode-II cracks and can form/grow during the sintering process when particles in the entire interconnect structure have coalesced. For the simple delamination geometry in Figure 4B, we can estimate the stress in the interconnect upon sintering. We assume that the delaminated section on the left of the separation in Figure 4B is stress-free, with the separation at the interface being between Ag-Ag ($G \approx 1$ J m^{-2}) and Ag-PI ($G = 30$ J m^{-2}) where G is the crack energy release rate. Estimating the displacement of 0.5 µm (half the separation between the two sections of the interconnect) for a crack length of 6 µm, a strain of about 8% is estimated. This strain level corresponds to stress due to sintering in the film to be tens of MPa, assuming that delamination cracking forms during sintering well after the solvent has evaporated.

2.2. Interconnect Microstructure and Conductivity

2.2.1. Microstructure

To assess the effect of processing conditions on the microstructure of the interconnects, we analyzed FIB cross-section images of several samples processed under the conditions shown in Table 1. **Figure 6**A–C shows the microstructure of the samples sintered in vacuum, 101 kPa N_2, and air environments (the conditions in experiment #2, #8, and #11 in Table 1), respectively. These samples were supplied with identical heating profiles and vary only in the ambient conditions. It is clear that the microstructures are significantly different, and the presence of oxygen has catalyzed the breakdown and removal of the organic ligands and binders to promote sintering. Very limited necking and particle size comparable to the original ink is observed in the microstructure of the vacuum sintered sample in Figure 6A, indicating poor sintering. The microstructure in Figure 6B (dried and sintered under N_2 environment) shows an increase in average particle size and a higher degree of NP necking compared to the vacuum sintered condition. This effect may be partly due to more uniform heating due to the inclusion of convection as an additional heat transfer mechanism vs that in vacuum. Further, there may be trace amounts of oxygen present as the oven was sealed only under vacuum pressure. The microstructure in Figure 6C is for the sample sintered in air, showing a significant increase in necking and average grain size indicating increased sintering. Along with the increased particle size and necking, the conductivity of the samples represented in Figure 6A–C increased and was 0.28%, 16%, and 67% of bulk silver, respectively.

Figure 6D–F shows microstructure for the samples where drying was performed under atmospheric conditions (process conditions for experiment #15, #18, and #13 of Table 1, respectively), The samples in Figure 6D,E were then sintered in vacuum at 200 and 300 °C, respectively; while the sample in Figure 6F was sintered in air at 200 °C. Note that

 © 2022 The Authors. Advanced Materials Technologies published by Wiley-VCH GmbH

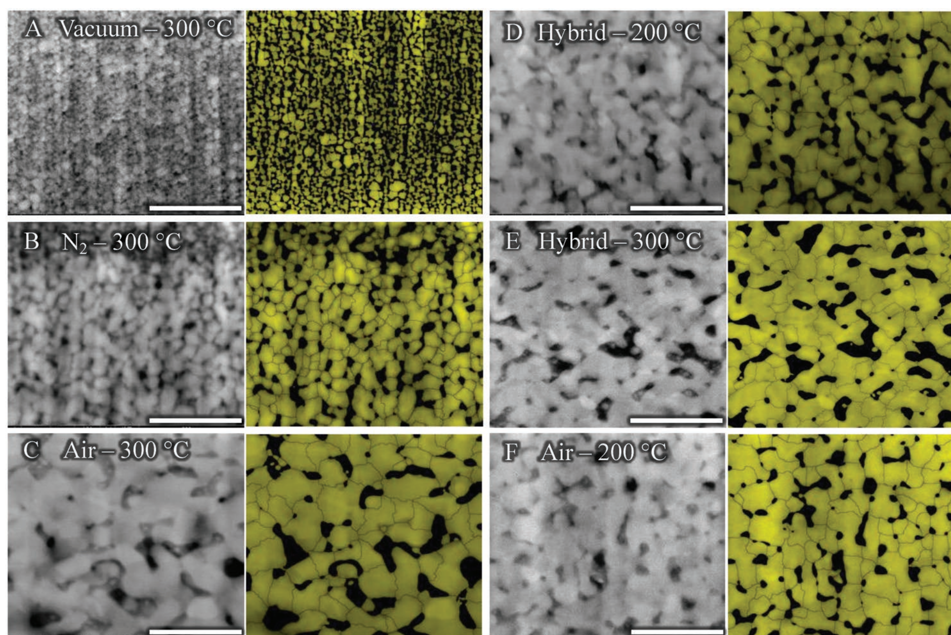

Figure 6. Microstructure of various key sintering process conditions and corresponding masks used for image analysis. A–C) Comparison of different sintering atmospheres up to 300 °C where A) is vacuum condition (experiment #2), B) is N_2 at ambient pressure (experiment #8), and C) is air at ambient pressure (experiment #11). D,E) Comparison of the D) hybrid process up to 200 °C (experiment #15), to the E) hybrid process up to 300 °C (experiment #18). F) The air-only condition up to 200 °C (experiment #13) is shown to compare to C) and D). The micrographs have the same magnification and scale bars are all 500 nm.

the microstructure of Figure 6E is for a sample printed on the PDMS substrate and the others are for samples printed on Si substrate. All the processes shown in Figure 6A–C,F, however, are unable to produce 3D printed interconnects directly on PDMS as the full vacuum and inert N_2 environment causes cracking in the Ag, while air exposure over 200 °C destroys the underlying PDMS substrate. The hybrid air/vacuum processes shown in Figure 6D,E were found to be fully compatible with the PDMS and exhibited no cracks, while showing high conductivity and a similar microstructure to the samples sintered under air.

2.2.2. Ink Composition and Process Development

The effect of different environments on the sintering of Ag NPs was investigated by Lu et al. over a series of publications,[31–33,50] where a silver NP paste was used for chip bonding on a Cu substrate in both reactive and inert environments. They determined that the removal of the organic ligands and binders to promote sintering of the NP was best performed in the presence of oxygen, but a formic acid vapor was also able to catalyze the breakdown of the organics without oxidizing the Cu substrate. In the current work, the metal NP ink undergoes several steps before becoming electrically conductive as shown in Figure 5. The composition of the ink, shown in the inset of Figure 5A, is an important factor in determining the conditions under which these steps occur. Typically, metallic nanoparticle inks have a short-chain organic ligand bonded directly to surface of the NPs to aid in the stability of the inks and reduce agglomeration before they are printed. The reduction of surface area can drive sintering at room temperature if the NPs are able to come in contact with each other; however, the ligands on the surface prevent that from occurring.[17] In addition to the ligands on the NP surface, long-chain polymers called binders are added to the ink to aid in cohesion to suppress cracking described in Section 3.1 as well as adhesion to aid in binding to the substrate. Solvents are then added to reach the desired viscosity for printing; the ink used in this study contains both water and ethylene glycol. The concentration and chain length of ligands and binders in metallic NP inks and solvents to optimize for low temperature sintering to achieve high conductivity remains a rich and active area of study.[22]

The first step after printing metallic NP inks is to remove the solvent by drying as shown in Figure 5B. Densification occurs through volume loss as the solvent evaporates and the NPs redistribute. This step is where capillary pressure can cause the cracking described above. The next step is to sinter the NPs to create a conductive film as shown in Figure 5C. This happens in several steps as the ligands are removed or displaced and the NP surfaces come in contact, while the surface diffusion causes coalescence and necking, and finally, grain growth. The thermal treatment provides the energy to drive the entire process and in general, larger grains and higher density requires higher energy.

A thermogravimetric analysis (TGA) was performed on the ink used in the current work under both air and 101 kPa N_2 environments at 10 °C min^{-1} to investigate the differences in weight loss between the two atmospheric conditions as shown in **Figure 7**. The TGA clearly shows an initial sharp drop in weight of the ink likely due to the evaporation of the solvents

© 2022 The Authors. Advanced Materials Technologies published by Wiley-VCH GmbH

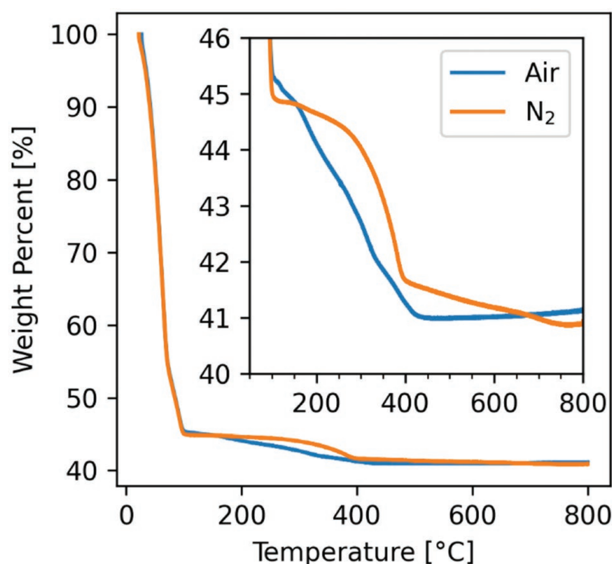

Figure 7. Thermogravimetric analysis of silver nanoparticle ink in nitrogen and air. The inset graph shows the weight loss of the ink after the solvent has been removed showing the dependance of binder and ligand removal on the sintering environment.

(to ≈45 wt%). After the sharp initial drop and as temperature rises from ≈150 to 430 °C, the ink weight in air continues to drop in a linear fashion, which is associated with the decomposition and removal of the organic ligands and binders. This is followed by a rise in the weight, likely due to the oxidation of Ag. In the N_2 environment, on the other hand, the ink displays a slow but accelerating weight loss beginning at ≈175–400 °C followed by a linear drop to 800 °C. The data, along with the microstructure seen in Figure 6A–C, indicate that oxygen is instrumental for the removal of the organics and is important for sintering of the Ag NPs. The TGA data in Figure 7 indicate that the ligand and binder burnout processes begin at ≈150 °C in air for the ink used in this study. However, the onset of burnout processes varies across different ink compositions and can be as high as 350 °C.[31] The maximum curing temperature for PDMS in air is 150 °C,[51] which informs a process window in air where the PDMS substrate may remain undamaged and the burnout of organics in the ink can begin to result in high conductivity interconnects.

To test the above hypothesis, the maximum drying temperature was increased to 150 °C from 120 °C in air, followed by a high temperature treatment under vacuum to promote further sintering as shown in Figure 2B. This initial drying step, performed under air, also has the added benefit of reducing cracking due to the rapid evaporation of solvents under the vacuum condition (see Section 3.1). Process conditions in experiment #14–18 (Table 1) use this hybrid sintering technique and can reach conductivities as high as 56% of bulk Ag when sintered at up to 300 °C (process condition for experiment #14 in Table 1). When printed directly onto PDMS under the same condition up to 300 °C (condition for experiment #18 in Table 1), the conductivity is 43% and it is 37% when sintered up to 200 °C (condition for experiment #17), indicating that the additional layer of PDMS affects the conductivity. Furthermore, there is an increase in conductivity from 25% to 37% of bulk Ag when the ramp rate to maximum temperature is decreased from 5 to 0.5 °C min^{-1}, indicating that increased time at sintering temperatures results in higher conductivity, which has been noted in previous studies.[11,52] Process conditions of experiments #12 and #13 in Table 1 comprised drying and sintering in air up to 200 °C and have very high conductivities up to 64%, which is comparable to air sintering up to 300 °C (which is 67%). Previous studies have reported a retention of stretchability of PDMS after exposure to 200 °C in air with a slight reduction in the maximum strain that the PDMS can withstand.[53] However, cracking in the PDMS was observed in our samples cured in air up to 200 °C (same as process conditions in experiment #12 and #13 in Table 1). A similar trend is shown in our previous work, where PDMS remains stretchable after thermal treatment in vacuum up to 300 °C but shows a decrease in maximum strain before failure compared to PDMS taken to 200 °C under vacuum. Therefore, an engineering tradeoff continues to exist between high conductivity of the sintered interconnect and retention of stretchability of the substrate, but the hybrid processes (#14–18 in Table 1) described in this work extend the process boundaries to achieve high conductivity traces with 3D features printed directly onto a stretchable substrate.

2.2.3. Modeling Conductivity with Microstructure Data

The microstructures of the printed silver interconnects shown in Figure 6A–C show increased necking and particle coalescence with sintering in vacuum, in N_2 at atmospheric pressure, and air at atmospheric pressure. The conductivities of the samples with microstructures shown in Figure 6A–F are given in **Table 2**. Several methods have been developed to predict the conductivity of porous solids based on microstructural characteristics. Maxwell's effective medium theory and Bruggeman's correlation may be the most widely used models as they employ only the relatively simple measurement of volume fraction of the material to determine the effective conductivity relative to the bulk material properties.[54] However, with availability of additional data such as the tortuosity of the conducting phase or grain size of the crystalline solid, more detailed models can be used. Rosker et al.[55] recently proposed a multiscale model that modified Maxwell's effective medium theory to include grain boundary scattering and gives

$$\frac{\kappa_{eff}}{\kappa_{bulk}} = \frac{\lambda_{gb}}{\lambda_0 + \lambda_{gb}}\left(\frac{2\phi}{3-\phi}\right) \tag{4}$$

where κ_{eff} is the effective conductivity, κ_{bulk} is the bulk conductivity (6.3×10^7 S m^{-1} for silver), λ_0 is the mean free path of an electron in the conductor (53 nm at 300 K for silver), ϕ is the volume fraction described above, and λ_{gb} is the characteristic line of sight distance for an electron moving across a grain in the ballistic transport regime. The characteristic line of sight is determined by the average length to cross the grain, and we follow the procedure by Rosker to approximate grains as spheres and use the average chord length of a sphere as λ_{gb}. The microstructure images in Figure 6 are analyzed with ImageJ[56]

© 2022 The Authors. Advanced Materials Technologies published by Wiley-VCH GmbH

Table 2. Results of microstructure image analysis and comparison of measured conductivity to the microscale conductivity model described by Rosker et al., and tortuosity model. The characteristic length of the particle was averaged over at least 45 particles using ImageJ. The tortuosity factor was averaged over both *x* and *y* directions for four different sections of the image. The volume fraction was averaged over the eroded and dilated particle size in ImageJ. The measured conductivity was averaged over four samples.

Process description and number		Volume fraction		Characteristic length		Tortuosity factor		Multiscale model conductivity		Tortuosity model conductivity		Measured conductivity	
[–]	[–]	[%]	Std dev	[nm]	Std dev	[–]	Std dev	[%] of bulk Ag	Std dev	[%] of bulk Ag	Std dev	[%] of bulk Ag	Std dev
Vacuum – 300 °C	2	61	±9	15	±4	10	±5	12	±4	6.2	±3	0.28	±0.02
N_2 – 300 °C	8	84	±2	35	±12	1.5	±0.1	31	±10	56	±4	16	±7
Air – 300 °C	11	82	±1	67	±21	1.45	±0.07	42	±13	57	±3	67	±2
Hybrid – 200 °C	15	82	±2	50	±17	1.64	±0.04	37	±12	50	±2	39	±1
Hybrid – 300 °C	18	83	±1	50	±16	1.42	±0.11	37	±12	58	±5	43	±5
Air – 200 °C	13	87	±2	57	±15	1.35	±0.04	42	±11	64	±2	59	±5

software by thresholding and water shedding to determine individual grains and are shown as the yellow mask images in Figure 6. The "analyze particles" function in ImageJ is then able to return the volume fraction, grain area, and perimeter.

In addition to using the multiscale model, conductivity was modeled using the standard definition for the tortuosity factor, τ, using the following relationship[57]

$$\frac{\kappa_{\text{eff}}}{\kappa_{\text{bulk}}} = \frac{\phi}{\tau} \tag{5}$$

The tortuosity factor was determined using TauFactor[58] with the same mask images in Figure 6 without the grain boundary lines, averaged over both horizontal and vertical directions in multiple areas of the image. The tortuosity measurement results in the same tortuosity factor that can be determined from Bruggeman's correlation, which is not independent of volume fraction.

The effective interconnect conductivity was determined utilizing both methods described in Equations (4) and (5) and compared against the measured conductivity. The full results are detailed in Table 2, and select conditions are shown in Figure S3 (Supporting Information). The model results in Table 2 show that both the multiscale model and the tortuosity factor model overpredict the conductivity for samples sintered under vacuum and 101 kPa N_2 environments, while the air sintered sample is underpredicted by both the models. The microstructure images for samples sintered under vacuum and N_2 environments in Figure 6 show more individual rounded particles rather than the porous, but continuous, grain structure shown by the air-sintered sample. The lack of necking between particles could be due to the remaining ligands and binders in the microstructure, preventing further sintering of the particles, which presents an additional scattering mechanism that is not captured by either model and may explain the overpredicted conductivity of the vacuum and N_2 sintered samples. The air sintered sample, on the other hand, is underpredicted by both the models, but the tortuosity model (57% of bulk Ag) is closer to the measured conductivity (67% of the bulk) compared to the multiscale model, which predicts an interconnect conductivity of only 42% of bulk Ag. This less accurate prediction by the multiscale model may be due to the assumption of spherical particle shape made in both the microscale and macroscale sections of the model, whereas the tortuosity factor is numerically determined directly from the microstructure. The hybrid air/vacuum sintering process falls in between the predicted conductivity of the multiscale and tortuosity models and is within a standard deviation of the multiscale model as shown by Table 2. These correlations have been known and investigated for many years, yet an accurate general model is still an elusive goal of active research in the battery, fuel cell, and geology communities.[54] Despite the large discrepancies between predicted values and measured values of conductivity, the trend of increasing conductivity with increasing grain sizes and decreasing porosity and tortuosity is captured by both models, indicating a dependence of the conductivity on the microstructure.

2.3. Shear Test of 3D Pillars

The strength and reliability of the 3D printed pillars are important in practical applications and were investigated by developing a shear test apparatus shown in Figure S4 (Supporting Information). Both hollow circular and tapered pillar geometries were tested. In addition, for each pillar type, process conditions that resulted in cracking at the pillar base and crack-free pillars were also evaluated. The maximum stress during the shear test for both geometries fabricated under each process condition are shown in **Figure 8**A. Clearly, the samples dried and sintered in vacuum were weakest with lowest failure stress: 9.2 MPa for the tapered pillar, and only 1.8 MPa for the circular pillar. The reason for the lower failure stress for this process condition is likely to be the presence of cracks underneath the pillars (Figure 3D; and Figure S2D, Supporting Information). The post failure scanning electron microscope (SEM) images in Figure 8B show a difference in failure mode between the pillars fabricated under vacuum and N_2 environments (with underlying cracks) where sections of the pad underneath the pillar remain intact. This contrasts with the pillars fabricated in air and hybrid conditions, where failure occurred at the interface of PI and Ag rather than within the Ag structure. The air and hybrid process conditions resulted in larger failure stress of 18.6 and 17.2 MPa, respectively, for the taper pillars, and 36.1 and 36.3 MPa, respectively, for the hollow circular pillars. The failure stress for hollow circular pillars was less than that for

© 2022 The Authors. Advanced Materials Technologies published by Wiley-VCH GmbH

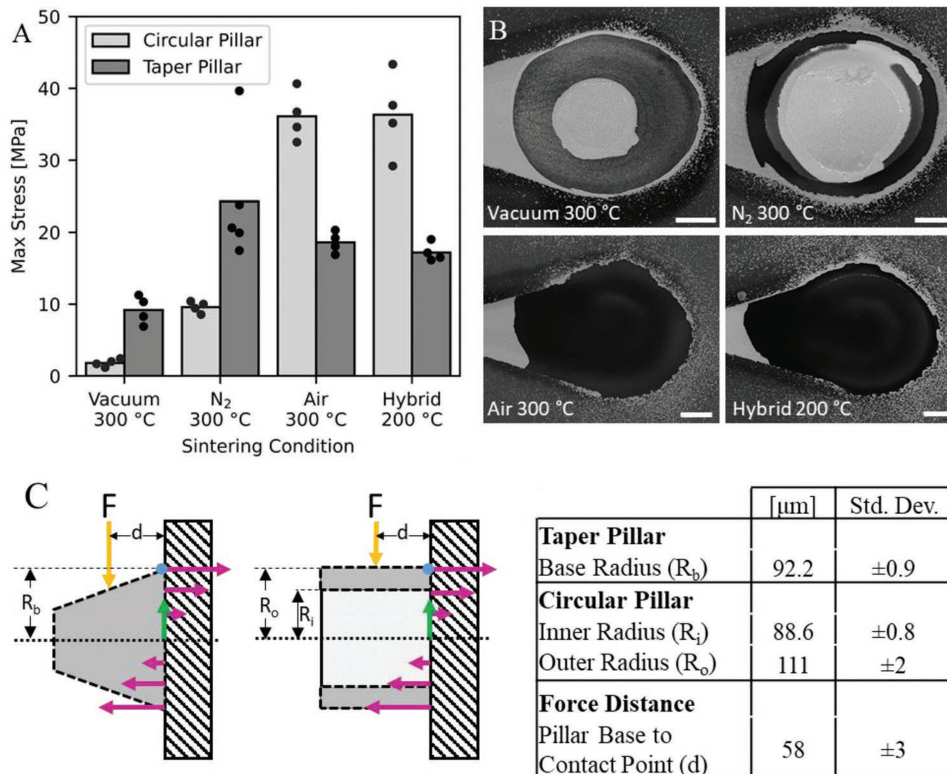

	[µm]	Std. Dev.
Taper Pillar		
Base Radius (R_b)	92.2	±0.9
Circular Pillar		
Inner Radius (R_i)	88.6	±0.8
Outer Radius (R_o)	111	±2
Force Distance		
Pillar Base to Contact Point (d)	58	±3

Figure 8. Maximum stress developed at pillar base preceding failure, and post failure images of circular pillars. A) The mean of the data points shown are plotted by the bars for both the circular pillar and taper pillar geometries. B) SEM of circular pillar failure surfaces are shown for the same conditions shown in the chart. Scale bars are 50 µm. C) Schematic of force application to both the taper pillar and the circular pillar. The purple and green arrows schematically indicate the bending and shear stresses experienced by the pillar. The table shows the average of three measurements of as-printed pillar geometry from SEM and optical images that was used to determine the maximum stress in the pillar (blue point shown at the pillar base), which is plotted in A).

taper pillars for both the nitrogen and vacuum environments, which contrasts with the crack-free process conditions where the circular pillar geometry had the largest failure stress. This indicates that the circular pillar geometry can withstand higher applied stresses under ideal process conditions but is more sensitive to cracking at the base. Additionally, the hybrid sintering process to 200 °C resulted in the same mechanical response in the pillars compared to the air sintering process at 300 °C and survived stresses approaching the yield stress of bulk silver in the case of the circular pillar geometry.

2.4. 3D Pillars for Packaging of Fully Encapsulated Crack-Free Interconnects

A process to achieve high-conductivity 3D printed interconnects compatible with a stretchable PDMS substrate has been described in Sections 2.1–2.3 and can be utilized to print directly onto a PDMS substrate. For improved robustness, these interconnects can be further encapsulated in another layer of spin-cast PDMS as shown in Figure 1B. Pillars allow for connections to external circuitry or direct contact to skin, for example to be used as an electrode for health monitoring applications. As described in the fabrication section, Dynasolve was used for a timed wet etch of the residual PDMS film covering the tips of the pillars after spin coating. The measured etch rate was 0.5 ± 0.2 µm s^{-1} tested across four samples. Images of exposed pillar tips after etching, along with profilometer and resistance plots are shown in **Figure 9**. An SEM of each of the hollow and tapered pillars after the etch step are shown in Figure 9A for the hollow pillar and Figure 9B for the tapered pillar. The pillars shown in Figure 1D–G are between 150 and 200 µm tall, while the bottom and top layers of PDMS are each around 30 µm thick, resulting in a total PDMS thickness of 60 µm. This would leave 90–140 µm of the tips of the pillars above the PDMS encapsulation. However, the uncured PDMS is spin-cast onto the substrate and its viscosity creates a meniscus in the PDMS from the pillar toward the flat plane of the substrate. Stylus profilometer scans for both the hollow and tapered pillar were performed in Figure 9B,D. For the hollow pillar (Figure 9B), ≈25 µm of the tip of the pillar appears to be exposed from the top layer of PDMS with the meniscus occurring across 75% of the height of the pillar. Similarly, for the profilometer scan of the tapered pillar (Figure 9D), 20–40 µm of the tip of the pillar is exposed from the top layer of PDMS, and again there is a meniscus occurring across 75% of the height of the pillar.

Figure 9F represents measurements of the average of the resistance across each of the hollow and tapered pillars for samples with experimental condition #17 in Table 1, which includes

© 2022 The Authors. Advanced Materials Technologies published by Wiley-VCH GmbH

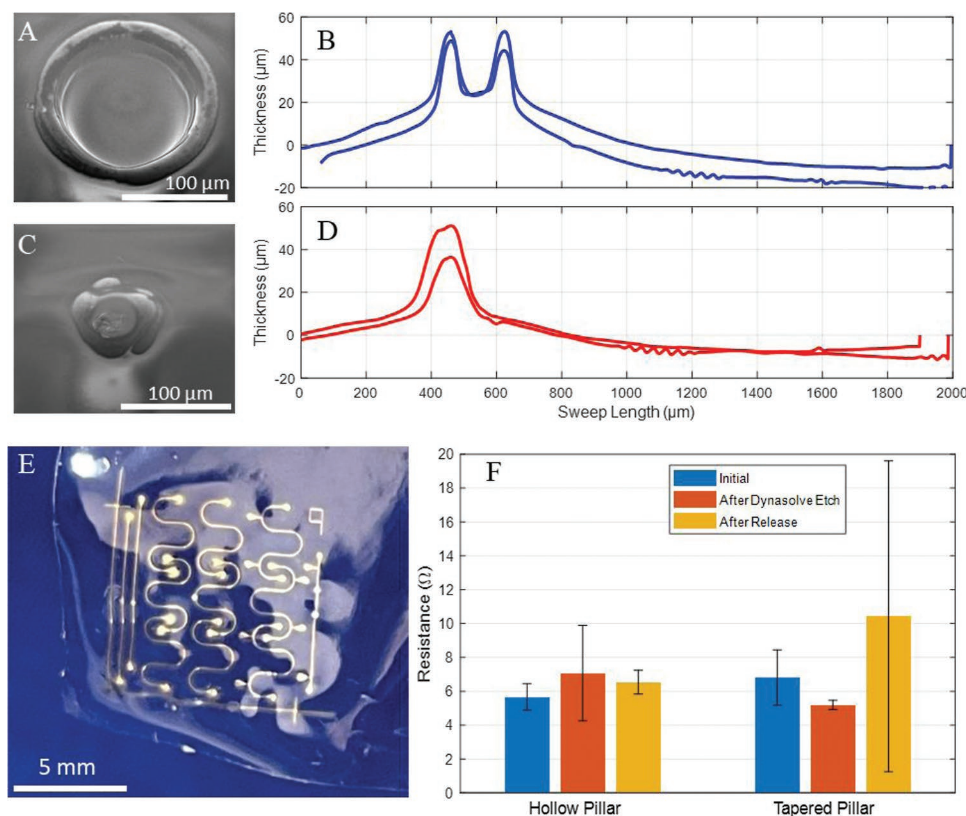

Figure 9. Encapsulation in PDMS and release from handle substrate. A) SEM image of encapsulated straight hollow pillar and C) taper full pillar with the tip exposed after the etching step to remove the thin top layer of PDMS. Profile scan of the exposed B) straight hollow pillar and D) taper full pillar showing ≈ 30 µm height of exposed silver extending from the PDMS to make electrical connection. E) Released sample with retained flexibility, and F) Resistance measurements throughout process steps averaged over four samples. “Initial” is prior to the second PDMS spin coating. Resistance is measured from pillar to pillar, and exposed pillar tips are shown in A) and C).

a PAA release layer, along with Ag traces insulated with PI and fully encapsulated in PDMS. The error bars represent one standard deviation apart from the average across four traces. A first resistance measurement was taken after sintering the Ag and curing the top layer of PI. Further resistance measurements were taken after spin-casting the top layer of PDMS and etching the PDMS residue above the pillars with Dynasolve. And finally, the resistance was measured after releasing the sample by using saline to dissolve the PAA release layer (shown in Figure 9E). The test structures required two-point resistance measurements. Overall, the resistance values remained consistent across each of the fabrication steps with some variability due to inconsistent probe placement across the tops of the pillars and uneven placement of the sample.

To test the functionality of exposed pillars as external connection points and demonstrate the stretchability of our interconnects, two meandering samples were fabricated following the hybrid condition to 200 °C shown in Figure 2B. The interconnect was connected to two separate external connection points at both ends to facilitate resistance measurements using a four-point probe during stretching. The samples were then cyclically stretched to 5%, 20%, and 30% strain, and the results are shown for one of the samples in Figure S6 (Supporting Information). The resistance deviated only 2% from the unstretched initial value during the cyclical stretching. The mechanical response was also consistent throughout the cyclical loading as shown in Figure S6A–C (Supporting Information). Additionally, a finite element analysis was performed to investigate the performance of the exposed pillar and stiffness gradient under 30% global strain and is detailed in Figure S8 (Supporting Information). The silver pillar experiences a maximum stress of 16.5 MPa, which is below the maximum stress preceding failure measured in both the hollow circular pillar and the tapered pillar under air and hybrid conditions shown in Figure 8. While the pillar experiences relatively low stress, the PDMS at the interface with the PI experiences a high strain indicating that the PI layer reduces the strain gradient at the pillar interface and the global strain is accommodated primarily by the stretchable PDMS and interconnects as intended.

The final released sample is shown in Figure 9E. We note a mismatch in the thermal treatment for the bottom and the top layer of PDMS in our interconnect system. The bottom layer of PDMS undergoes several high temperature thermal treatments for curing PI and sintering the Ag layers, while the top layer of PDMS experiences a curing treatment and a short drying step after Dynasolve etching, both at 100 °C. As a result, in stretching applications, the bottom and top layers of PDMS are expected to have different elastic moduli and maximum strain-to-failure. The bonding between the top and bottom PDMS layer was tested using ASTM D3359

 © 2022 The Authors. Advanced Materials Technologies published by Wiley-VCH GmbH

Tape Adhesion Test standard (see the Experimental Section for test details). Despite the differences in the thermal histories of the two PDMS layers, no delamination was observed during the adhesion test as seen in Figure S7 (Supporting Information).

3. Conclusion

AJP is utilized to fabricate 3D printed interconnects fully embedded in a stretchable substrate with external connection points with various pillar architectures. A hybrid sintering process of a drying step conducted in air at 150 °C, followed by a high temperature treatment in vacuum is shown to preserve the stretchable substrate, while producing crack-free and highly conductive 3D interconnects up to 56% of bulk Ag. Inert and vacuum environments are shown to produce cracking during drying due to increased inter-particle capillary force from rapid solvent evaporation. Additionally, organic ligands and binders present in Ag nanoparticle inks are shown to be removed more effectively in air at temperatures of 150 °C and above relative to an inert N_2 environment. The microstructure differences and increased conductivity of interconnects sintered under air relative to N_2 and vacuum environments further evidences the removal of the organics in the ink to be the cause of lower conductivity. A hybrid thermal process was developed where the low-temperature air drying step reduces the capillary force that initiates cracks and increases the removal of the organics in the Ag nanoparticle ink during, and the high-temperature sintering step under vacuum increases the conductivity while preserving elastic characteristics of the underlying PDMS.

These findings are suitable for applications in soft robotics, human machine interfaces, and health monitoring devices. Toward the application of health monitoring devices, the exposed silver pillars could be used as a dry electrode to contact the skin, or they could be utilized as vias enabling multiple printed electronic layers. Interfacing to external circuitry can be achieved using low temperature solder (which uses temperatures well below the thermal treatment profile peaking at 200 °C), silver paste or paint, or conductive tape. Incorporating multiple different types of functional components, as well as routing to multiple layers via the 3D pillar geometry is the aim of future work.

4. Experimental Section

Materials: The PDMS material (Sylgard 184, Dow Corning Corporation, Midland, MI) was prepared by mixing base elastomer and curing agent at a ratio of 20:1 by weight followed by degassing to remove bubbles. The interconnect conductor and pillars were fabricated using silver nanoparticle (NP) ink (Prelect TPS 50, Clariant, Frankfurt, Germany). The nanoparticle size in the ink was 30–50 nm, while the silver particle loading in the ink was 40 ± 2 wt%. The ink was diluted with deionized water at a ratio of 3:1 (ink:water) by volume prior to printing. The PI precursor resin (PI 2574, HD MicroSystems, Parlin, NJ) was mixed with N-Methyl-2-pyrrolidone (NMP) as a solvent at a ratio of 2:3 by volume.

Sample Fabrication: The process steps to create the samples shown in Figure 1 are described below. First, the mixed PDMS base and curing agent was spin-cast onto a silicon wafer having a PAA, (Polysciences, Warrington, PA) release layer following the procedure outlined in the earlier work.[28] The PDMS was cured at 100 °C for 1 h. The AJP (AJ 300 Optomec Inc, Albuquerque, NM) was then used to print the PI and silver interconnects. The AJP has pneumatic and ultrasonic atomizers that convert the ink into aerosol droplets which is carried by N_2 to the print head where the N_2 sheath gas is capable of focusing the aerosol stream to print features down to 10 µm depending upon the nozzle size and gas flow parameters.[59] To print PI, the pneumatic atomizer was used along with a 300 µm diameter nozzle, a sheath gas flow rate of 80–100 sccm, a carrier gas flow rate of 40–50 sccm, and a platen temperature of 60 °C. The PI was then cured according to the conditions specified in Table 1 for a specific experiment #. Silver nanoparticle ink was then printed directly onto the cured PI layer utilizing the ultrasonic atomizer and a 150 µm diameter nozzle, a sheath gas flow rate of 45–50 sccm, a carrier gas flow rate of 25–30 sccm, and a platen temperature of 60 °C. After sintering the silver (under the same condition as that for PI below - Table 1), another layer of PI precursor was printed on top of the silver to encapsulate the silver interconnects in PI. The top PI layer was then cured, under the same processing conditions as the bottom PI layer and silver layer. Finally, a top layer of PDMS was spun on top of the printed sample using the same procedure as the bottom PDMS layer to fully encapsulate the electrical traces but leave the tips of the pillars exposed. The top PDMS is then cured under the same conditions as the bottom PDMS. To remove any residual PDMS on the tips of the pillars, a 10 s soak in Dynasolve (Versum Materials, Tempe, AZ), followed by 5 min soak in an isopropyl alcohol bath, and a drying step at 100 °C for 30 min was performed. The stretchable sample was then released from the Si handle substrate via saltwater soak for 24 h and rinsed with DI water.

Sample Characterization: Sample interconnect resistance was measured with a four-point probe at the locations shown in Figure 1C (2401 SourceMeter, Keithley Instruments, Cleveland, OH). Pillar to pillar resistance was measured with two-point probe at the locations shown in Figure 1C. Trace cross-sectional profiles were measured with profilometer scans (Dektak 3, Bruker Corporation, Billerica, MA) to determine conductivity of the sintered silver along with the resistance measurements. The Ag cracks and microstructure were characterized with SEM images (Quanta 600, FEI, Hillsboro, OR) utilizing focused ion beam (FIB) (Nova Nanolab 600, FEI, Hillsboro, OR) cutting to expose the cross section of cracks and internal microstructure of the traces and pillars, and ImageJ[56] and TauFactor[58] were used to analyze the images. Additionally, thermogravimetric analysis (TGA) (Q50, TA Instruments, New Castle, DE) was performed on the Ag NP ink in both air and nitrogen to investigate the binder and surfactant removal under inert and reactive environments.

The pillar shear test set-up is shown in Figure S4 (Supporting Information). In this setup, the samples were loaded horizontally on a four-axis microstage to allow for their precise positioning under the load cell (LSB200, Futek, Irvine, CA) and contact head as shown in Figure S4B (Supporting Information). The samples were positioned so that the contact head would apply the load on the pillar about 50 µm from the pillar base as shown in Figure S4A (Supporting Information). These optical images were analyzed with ImageJ to measure the distance from the pillar base to the contact point for use in the stress calculations shown in Figure 8. The load cell was mounted on a linear stage (X-LSM025, Zaber Technologies Inc., Vancouver) and driven at a constant rate of 0.5 µm s^{-1}. A MATLAB (MathWorks, Natick, MA) script was used to record both the displacement and load simultaneously. The maximum measured force for each condition is plotted in Figure S5A (Supporting Information). The equivalent von Mises stress at the base of the pillars is reported in Figure 8 and was determined by analyzing SEM images with ImageJ to measure the dimensions of the pillars as shown in Figure 8C. SEM images were taken post failure and are shown in Figure S5B (Supporting Information) for the taper pillar geometry.

Tensile testing of fully embedded interconnect as reported in Figure S6 (Supporting Information) was carried out using a universal tensile tester (Instron 5969, Norwood, MA) and four-probe resistance measurement (2401 SourceMeter, Keithley Instruments, Cleveland, OH). Electrical connections were made with the fully embedded

© 2022 The Authors. Advanced Materials Technologies published by Wiley-VCH GmbH

meandering interconnects through exposed pillar tips shown in Figure 9A. The sample was cycled at 5%, 20%, and 30% strain at a rate of 12.5 mm min^{-1} while simultaneously recording resistance, force, and displacement. The sample geometry, shown in Figure S6D (Supporting Information), is a scaled down type-C specimen shape described in ASTM D412,[60] and the cyclical strain values were chosen following the suggestions of stretchable device design from the Semiconductor Research Corporation.[61] The strain is reported as the strain developed in the testing region using the same method as in the previous work.[28]

Adhesion between the top and bottom PDMS layers was tested using ASTM D3359 Tape Adhesion Test (Test Method B – guidelines for 50–125 µm thick materials).[62] The bottom layer of 20:1 PDMS was spun cast, cured at 100 °C for 1 h, and treated with three heating profiles as shown in Figure 2B to replicate the curing and sintering conditions of PI and Ag. The top layer of 20:1 PDMS was spin cast and cured at 100 °C for 1 h. Cross sections following ASTM D3359 were cut using a sharp cutter (Curio, Silhouette America, Lindon, UT). A tape was then used according to the same standard to test the adhesion between the two PDMS layers.

Supporting Information

Supporting Information is available from the Wiley Online Library or from the author.

Acknowledgements

The project was financed in part by Highmark Health in Pittsburgh, a grant from the Commonwealth of Pennsylvania, Department of Community and Economic Development, and partial support from NSF Grant Nos. 1757117, DGE1252522, and DGE1745016.

Conflict of Interest

The authors declare no conflict of interest.

Data Availability Statement

The data that support the findings of this study are available from the corresponding author upon reasonable request.

Keywords

3D printing, aerosol jet printing, nanoparticle ink, reliable interconnects, stretchable electronics

Received: March 11, 2022
Revised: May 9, 2022
Published online:

[1] J. A. Rogers, R. Ghaffari, D.-H. Kim, *Stretchable Bioelectronics for Medical Devices and Systems*, Springer, Switzerland **2016**.
[2] M. Cianchetti, C. Laschi, A. Menciassi, P. Dario, *Nat. Rev. Mater.* **2018**, *3*, 143.
[3] C. Majidi, *Soft Rob.* **2014**, *1*, 5.
[4] H. U. Chung, B. H. Kim, J. Y. Lee, J. Lee, Z. Xie, E. M. Ibler, K. Lee, A. Banks, J. Y. Jeong, J. Kim, C. Ogle, D. Grande, Y. Yu, H. Jang, P. Assem, D. Ryu, J. W. Kwak, M. Namkoong, J. B. Park, Y. Lee, D. H. Kim, A. Ryu, J. Jeong, K. You, B. Ji, Z. Liu, Q. Huo, X. Feng, Y. Deng, Y. Xu, et al., *Science* **2019**, *363*, eaau0780.
[5] R. Herbert, S. Mishra, H. R. Lim, H. Yoo, W. H. Yeo, *Adv. Sci.* **2019**, *6*, 1901034.
[6] O.-H. Huttunen, T. Happonen, J. Hiitola-Keinänen, P. Korhonen, J. Ollila, J. Hiltunen, *Ind. Eng. Chem. Res.* **2019**, *58*, 19909.
[7] J. Perelaer, U. S. Schubert, *J. Mater. Res.* **2013**, *28*, 564.
[8] G. W. Huang, H. M. Xiao, S. Y. Fu, *Sci. Rep.* **2015**, *5*, 13971.
[9] A. Kamyshny, S. Magdassi, *Small* **2014**, *10*, 3515.
[10] Y. Choi, K. d. Seong, Y. Piao, *Adv. Mater. Interfaces* **2019**, *6*, 1901002.
[11] M. T. Rahman, J. McCloy, C. V. Ramana, R. Panat, *J. Appl. Phys.* **2016**, *120*, 075305.
[12] M. Sadeq Saleh, M. HamidVishkasougheh, H. Zbib, R. Panat, *Scr. Mater.* **2018**, *149*, 144.
[13] Y. Kim, X. Ren, J. W. Kim, H. Noh, *J. Micromech. Microeng.* **2014**, *24*, 115010.
[14] M. J. Renn, M. Schrandt, J. Renn, J. Q. Feng, *J. Microelectron. Electron. Packag.* **2017**, *14*, 132.
[15] M. T. Rahman, C.-Y. Cheng, B. Karagoz, M. Renn, M. Schrandt, A. Gellman, R. Panat, *ACS Appl. Nano Mater.* **2019**, *2*, 3280.
[16] J. Perelaer, B. J. deGans, U. S. Schubert, *Adv. Mater.* **2006**, *18*, 2101.
[17] D. Wakuda, M. Hatamura, K. Suganuma, *Chem. Phys. Lett.* **2007**, *441*, 305.
[18] R. Danaei, T. Varghese, M. Ahmadzadeh, J. McCloy, C. Hollar, M. Sadeq Saleh, J. Park, Y. Zhang, R. Panat, *Adv. Eng. Mater.* **2019**, *21*, 1800800.
[19] S.-H. Park, S. Jang, D.-J. Lee, J. Oh, H.-S. Kim, *J. Micromech. Microeng.* **2013**, *23*, 015013.
[20] S. Ma, V. Bromberg, L. Liu, F. D. Egitto, P. R. Chiarot, T. J. Singler, *Appl. Surf. Sci.* **2014**, *293*, 207.
[21] W. Shen, X. Zhang, Q. Huang, Q. Xu, W. Song, *Nanoscale* **2014**, *6*, 1622.
[22] L. Mo, Z. Guo, Z. Wang, L. Yang, Y. Fang, Z. Xin, X. Li, Y. Chen, M. Cao, Q. Zhang, L. Li, *Nanoscale Res. Lett.* **2019**, *14*, 197.
[23] Y. Arafat, I. Dutta, R. Panat, *Appl. Phys. Lett.* **2015**, *107*, 081906.
[24] Y. Arafat, I. Dutta, R. Panat, *J. Appl. Phys.* **2016**, *120*, 115103.
[25] S. Xu, Y. Zhang, J. Cho, J. Lee, X. Huang, L. Jia, J. A. Fan, Y. Su, J. Su, H. Zhang, *Nat. Commun.* **2013**, *4*, 1543.
[26] Y.-Y. Hsu, M. Gonzalez, F. Bossuyt, J. Vanfleteren, I. De Wolf, *IEEE Trans. Electron Devices* **2011**, *58*, 2680.
[27] N. Naserifar, P. R. LeDuc, G. K. Fedder, *Adv. Mater.* **2016**, *28*, 3584.
[28] D. Z. Tansel, J. Brenneman, G. K. Fedder, R. Panat, *J. Micromech. Microeng.* **2020**, *30*, 067001.
[29] M. S. Saleh, C. Hu, R. Panat, *Sci. Adv.* **2017**, *3*, e1601986.
[30] M. S. Saleh, C. Hu, J. Brenneman, A. M. Al Mutairi, R. Panat, *Addit. Manuf.* **2021**, *39*, 101856.
[31] J. G. Bai, T. G. Lei, J. N. Calata, G.-Q. Lu, *J. Mater. Res.* **2011**, *22*, 3494.
[32] H. Yan, Y.-H. Mei, M. Wang, X. Li, G.-Q. Lu, *J. Mater. Sci.: Mater. Electron.* **2019**, *30*, 9634.
[33] H. Zheng, D. Berry, K. D. T. Ngo, G.-Q. Lu, *IEEE Trans. Compon., Packag., Manuf. Technol.* **2014**, *4*, 377.
[34] S. Liu, Y. Li, S. Xing, L. Liu, G. Zou, P. Zhang, *Materials* **2019**, *12*, 1559.
[35] N. Dalal, Y. Gu, D. R. Hines, A. Dasgupta, S. Das, *J. Micromech. Microeng.* **2019**, *29*, 097001.
[36] D. J. Lee, J. H. Oh, H. S. Bae, *Mater. Lett.* **2010**, *64*, 1069.
[37] J. H. Prosser, T. Brugarolas, S. Lee, A. J. Nolte, D. Lee, *Nano Lett.* **2012**, *12*, 5287.
[38] G. W. Scherer, *J. Non-Cryst. Solids* **1989**, *109*, 171.
[39] W. P. Lee, A. F. Routh, *Langmuir* **2004**, *20*, 9885.
[40] A. F. Routh, W. B. Russel, *Langmuir* **1999**, *15*, 7762.
[41] J. Brenneman, D. Z. Tansel, G. K. Fedder, R. Panat, *Extreme Mech. Lett.* **2021**, *43*, 101199.

© 2022 The Authors. Advanced Materials Technologies published by Wiley-VCH GmbH

[42] A. F. Routh, *Rep. Prog. Phys.* **2013**, *76*, 046603.
[43] J. R. Greer, R. A. Street, *J. Appl. Phys.* **2007**, *101*, 103529.
[44] F. Juillerat, P. Bowen, H. Hofmann, *Langmuir* **2006**, *22*, 2249.
[45] J. M. Salamanca, E. Ciampi, D. A. Faux, P. M. Glover, P. J. McDonald, A. F. Routh, A. C. I. A. Peters, R. Satguru, J. L. Keddie, *Langmuir* **2001**, *17*, 3202.
[46] MEGlobal, *Physical Properties of Ethylene Glycol*, **2008**.
[47] K. Ando, M. Arakawa, A. Terasaki, *Chem. Lett.* **2016**, *45*, 961.
[48] Y.-Y. Su, A. Marsh, A. E. Haddrell, Z.-M. Li, J. P. Reid, *J. Geophys. Res.: Atmos.* **2017**, *122*, 12.
[49] M. Rusdi, Y. Moroi, H. Nakahara, O. Shibata, *Langmuir* **2005**, *21*, 7308.
[50] T. G. Lei, J. N. Calata, G.-Q. Lu, X. Chen, S. Luo, *IEEE Trans. Compon. Packag. Technol.* **2010**, *33*, 98.
[51] D. C. Company, *SYLGARD 184 Silicone Elastomer Kit Technical Data Sheet*, **2017**.
[52] J. R. Greer, R. A. Street, *Acta Mater.* **2007**, *55*, 6345.
[53] I. D. Johnston, D. K. McCluskey, C. K. L. Tan, M. C. Tracey, *J. Micromech. Microeng.* **2014**, *24*, 35017.
[54] B. Tjaden, S. J. Cooper, D. J. L. Brett, D. Kramer, P. R. Shearing, *Curr. Opin. Chem. Eng.* **2016**, *12*, 44.
[55] E. S. Rosker, M. T. Barako, E. Nguyen, D. DiMarzio, K. Kisslinger, D. W. Duan, R. Sandhu, M. S. Goorsky, J. Tice, *ACS Appl. Mater. Interfaces* **2020**, *12*, 29684.
[56] C. A. Schneider, W. S. Rasband, K. W. Eliceiri, *Nat. Methods* **2012**, *9*, 671.
[57] T.-T. Nguyen, A. Demortière, B. Fleutot, B. Delobel, C. Delacourt, S. J. Cooper, *npj Comput. Mater.* **2020**, *6*, 123.
[58] S. J. Cooper, A. Bertei, P. R. Shearing, J. A. Kilner, N. P. Brandon, *SoftwareX* **2016**, *5*, 203.
[59] M. T. Rahman, A. Rahimi, S. Gupta, R. Panat, *Sens. Actuators, A* **2016**, *248*, 94.
[60] ASTM, *D412 Standard Test Methods for Vulcanized Rubber and Thermoplastic Elastomers-Tension*, ASTM, West Conshohocken, PA **2021**.
[61] R. Mahajan, P. Brofman, R. Alapati, C. Hilbert, L. Nguyen, K. Maekawa, M. Varughese, D. O'Connor, S. Ramaswami, J. Candelaria, Semiconductor Research Corporation, Packaging Needs Document, https://www.src.org/program/grc/pkg/research-needs/2015/packaging.pdf **2015**.
[62] ASTM, *D3359 Standard Test Methods for Rating Adhesion by Tape Test*, ASTM, West Conshohocken, PA **2017**.

© 2022 The Authors. Advanced Materials Technologies published by Wiley-VCH GmbH